CrossMark

Structural, chemical, and electrical properties of ZrO$_2$/Ge system formed via oxidation/nitridation in N$_2$O gas ambient

Zhen Ce Lei[1] · Nor Ishida Zainal Abidin[1] · Yew Hoong Wong[1]

Abstract

The effects of oxidation/nitridation for 15 min at different temperatures (300–800 °C) on metal–oxide–semiconductor characteristics of sputtered Zr thin film based on Ge substrate in N$_2$O ambient have been systematically investigated. The crystallinity of the film were evaluated by X-ray diffraction analysis, Raman analysis, and X-ray photoelectron spectrometer. The crystallite size and microstrain of film were estimated by Williamson–Hall plot analysis. Optical microscope was used to examine samples surface condition and high-resolution transmission electron microscopy was carried out to investigate the cross-sectional morphology. GeO$_2$ was detected in samples with oxidation/nitridation temperature above 700 °C. A possible mechanism of Ge atomic diffusion and its rearrangement in ZrO$_2$ has been proposed and explicated.

1 Introduction

SiO$_2$/Si material structure has dominated the semiconductor industries for complementary metal oxide (CMOS) process for decades. The reason being SiO$_2$ has excellent insulating properties and low interface trap level density around the order of approximately 10^{10} cm^{-2} eV^{-1} with Si surface [1–4]. To improve device performance, the geometry of device has been shrank continuously for past few decades. Besides dimensions shrinkage, alternative material structures were also studied intensively [5, 6]. The paragraph below will give an in-depth explanation.

Looking at current Si substrate, to improve device performance, besides shrinking the channel length, another option is changing the material which has higher mobility than silicon. Comparing both essential devices which comprise p-MOSFET and n-MOSFET, the mobility of majority carrier of p-MOSFET is lower than its majority carrier of n-MOSFET. Hence, it is more essential to improve from p-MOSFET aspect [7]. Ge was selected in this study because it has the highest hole mobility in all of the known semiconductor materials [8]. The hole mobility of Ge is 1900 cm^2 eV^{-1} s^{-1}, more than 4 times compared with Si [9].

As newer-generation chip dimensions are shrinking, gate oxide thickness is reducing. However, SiO$_2$ encounters physical limitation with tunneling effect when thickness is down to 1.2 nm [10]. Therefore, alternative high κ materials were widely study as SiO$_2$ replacement, such as HfO$_2$, ZrO$_2$ [11], Sm$_2$O$_3$ [12], Nd$_2$O$_3$ [13], TiO$_2$ [14], Ta$_2$O$_5$ [15], Al$_2$O$_3$ [16], Y$_2$O$_3$ [17], and other. In this study, ZrO$_2$ have been selected for its high κ value, large-energy bandgap, and its stability in the form of cubic or tetragonal polymorphs [18]. Another benefit is the interfacial layer (IL) free between ZrO$_2$ gate dielectric and Ge wafer during thermal treatment [9] which will prevent electrical breakdown prematurely [19]. The phenomenon of IL free may due to the Ge diffusion into ZrO$_2$ dielectric [9]. The details of the behavior still remains an open question. A possible mechanism of Ge atomic diffusion and its rearrangement in ZrO$_2$ has been proposed and explicated in this paper.

Compared with the counterpart Si, Ge is considerably unstable at high-temperature process. As studied previously [20], it is observed that Zr/Ge was unstable at oxidation temperature above 600 °C at O$_2$ ambient. On the other hand, NO and N$_2$O are common gases used for oxidation and nitridation process in semiconductor industries [21]. N$_2$O is the preferred gas because it is less toxic as compared with NO [22]. Another reason for NO was not selected in this study because of its activation energies are lower than O$_2$. This study will focus on changing to N$_2$O ambient conditions where activation energies are higher than O$_2$ [23] and study the stability under different temperature.

✉ Yew Hoong Wong
yhwong@um.edu.my

[1] Department of Mechanical Engineering, Faculty of Engineering, University of Malaya, 50603 Kuala Lumpur, Malaysia

2 Experimental procedures

To prepare impurity-free samples, germanium wafer [n-type, (100)-oriented, 0.01–0.05 Ω cm, 1 cm × 1 cm] were dipped cleaned by hydrofluoric acid (HF) solution (1:50 HF:H_2O) and DI water. By using TF 450 physical vapor deposition (PVD) radio frequency (RF) sputtering system, metallic zirconium (Zr) film was sputtered from a Zr target (Kurt J. Lesker, USA, 99.999% purity) at room temperature. Pressure, RF power, and argon gas flow rate were set at 3×10^{-5} mbar, 170 W, and 25 cm³ min⁻¹, respectively. Experimental oxidation/nitridation temperatures were set at 300, 400, 500, 600, 700, and 800 °C using Carbolite CTF tube furnace. Samples of sputtered Zr on Ge wafer were placed into the tube furnace with N_2O flow rate of 150 mL min⁻¹ at each experimental temperature for 15 min. The oxidized/nitrided samples were cooled down in the tube furnace before removal.

The properties of the samples were characterized by various measurement methods which are as follows: film crystallinity was characterized using a PANalytical Empyrean X-ray diffractometer (XRD) system in the 2θ scan range from 10° to 80°. Copper radiation (Cu K$_α$) with wavelength (λ) of 0.15406 nm was used as X-ray source. The chemical compositions of the films were analyzed by X-ray photoelectron spectrometer (XPS) on AXIS ULTRA DLD (Al-Ka radiation). The X-ray tube was operated at 80 W. The analyzed area had a diameter of 300 μm. During XPS measurements, the pressure in UHV chamber was about 3×10^{-9} Torr. Survey scan was measured at 160 eV (energy resolution 1 eV per step) pass energy, this was for elemental analysis. Narrow scan (with high resolution) was measured at 20 eV (energy resolution 0.1 eV per step) pass energy, and it was for chemical states analysis. All data were recorded at a 45° take-off angle. To study geometry structure, film samples were sent for deposition of platinum (Pt) on the surface for protection from ion bombardment damage caused by the focused ion beam during lamella preparation. Followed by cross-sectioning using TECNAI G2 F20 high-resolution transmission electron microscope (HRTEM), the interplanar spacing (d) of the polycrystalline structure was measured from HRTEM images using ImageJ software. Olympus BX61 optical microscope were used to examine samples surface and the picture capture by Color view (soft imaging system).

To study the electrical properties of the films, MOS capacitor test structures with area of 300 μm × 300 μm were fabricated. Aluminum (Al 99.9995% purity, 100 nm; Kurt J. Lesker, USA) was sputtered through a mask using a TF 450 PVD RF sputtering system. The back side of the Ge was also sputtered with 100-nm-thick Al film to form an Ohmic back contact. BPW-800 8″ probe station with a Keithley 4200 semiconductor characterization system (SCS) were used to measure current–voltage (I–V).

3 Results and discussion

3.1 J–E and J–V characteristics

The J–E and J–V characteristics were used to study the effects of oxidation/nitridation temperature on the electrical properties of the samples. Figure 1 shows the J–E and J–V characteristics of samples oxidized/nitridation at various temperatures. For samples of 300, 400, 500, and 600 °C, the thickness of the dielectric will be discussed in Sect. 3.6, the J–E curve using left axis and bottom axis at which the arrows pointing indicates. In the results, all the samples shows typical J–E curve. The electrical breakdown fields were 6.0, 6.9, 5.7, and 5.7 MV cm⁻¹, respectively. Electrical characterization revealed that 400 °C samples yielded the highest electrical breakdown fields. For samples of 700 and 800 °C, due to lack of values of dielectric thickness, the J–V curve were shown in Fig. 1. The J–V curve using right axis and top axis at which the arrows pointing indicates. The 700 °C samples shows an almost short circuit in the J–V curve, and the 800 °C samples shows an almost open circuit in J–V curve measurement results. For further study, a physical analysis will be performed in next section.

3.2 Optical microscope analysis

Optical microscope was used to examine samples surface condition at various temperatures as shown in Fig. 2. Figure 2a shows the 300–600 °C samples, the surfaces were found to be smooth and free from defects. Figure 2b shows the 700 °C samples with scattered blisters. Figure 2c shows the 800 °C samples. For indication of surface
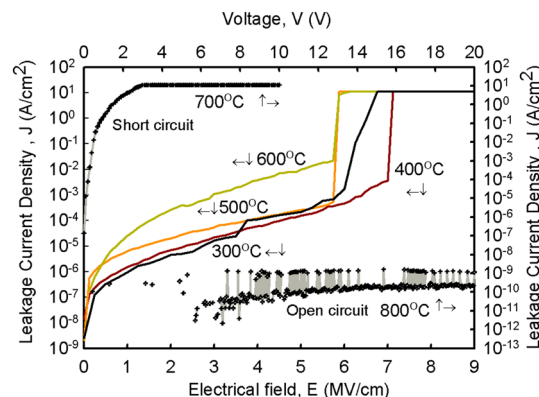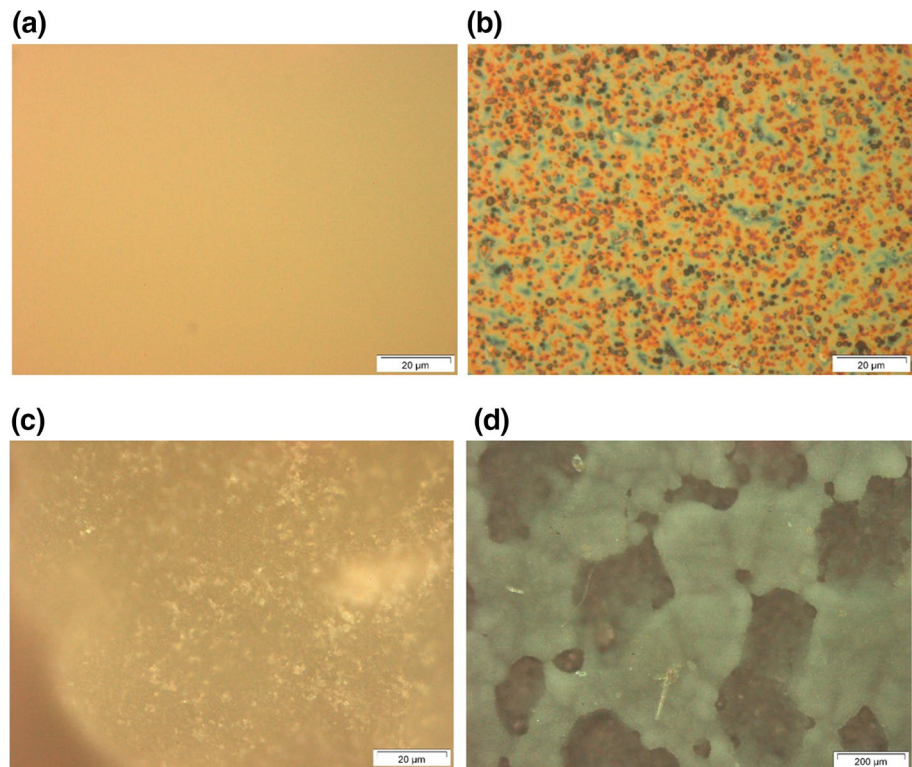

Fig. 1 J–E and J–V characteristics of samples oxidized/nitridation at various temperatures

Fig. 2 Optical microscope of samples surface. **a** Samples oxidized/nitridation at 300–600 °C, **b** samples oxidized/nitridation at 700 °C, **c** samples oxidized/ nitridation at 800 °C and **d** samples oxidized/nitridation at 800 °C with lower magnification

roughness, another lower magnification for sample 800 °C is shown in Fig. 2d.

Comparing 600 °C samples between N_2O ambient and O_2 ambient, the N_2O ambient samples were smooth and defect-free. This might be because the activation energies of N_2O is higher than O_2. For the 700 °C samples, the surface was similar for both N_2O and O_2 ambient. This could be results of similar reaction where N_2O or O_2 atoms diffused through the ZrO_2 layer, forming GeO_2 under N_2O or O_2 ambient. For 800 °C, Rough surface with uneven thick films on the sample were observed. There have been lack of literatures on the liquid state of Ge_3N_4. It has been reported that the Ge_3N_4 will decompose around 700–900 °C [24, 25]. In this study, based on the on the $J–V$ result and the OM analysis, it is assumed that some form of liquidation occurred during oxidized/nitridation at 800 °C and trapping GeO_2 in a form of solid powder on sample surface. These mixtures of liquid and powder further solidified on sample surface after cooling to room temperature. It was not observed at O_2 ambient. Hence, Ge_3N_4 was the possible material based on this assumption. Thus, explaining the difference between $J–V$ curve results where short circuits were observed for samples under O_2 ambient, and open circuits were observed for samples under N_2O ambient, all under 800 °C.

3.3 Raman spectroscopy analysis

Figure 3 shows the Raman analysis of oxidized/nitridation samples at various temperatures. The background noise for 700 and 800 °C samples were observed to be higher than the other samples during measurement. As a result, an extra Y-axis was added in Fig. 3 right hand sites. The peak that belonged to Ge was detected at 300 cm^{-1} for all samples. The peak that belonged to monoclinic ZrO_2 was detected at 181 and 346 cm^{-1} [26–28]. The peaks that belonged to tetragonal ZrO_2 were detected at 404 and 460 cm^{-1} [29].
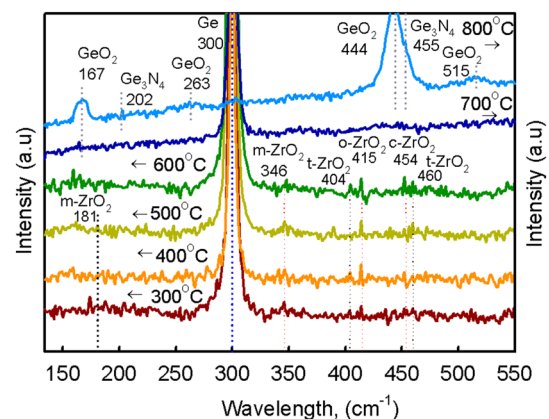

Fig. 3 Raman spectra of samples oxidized/nitridation at various temperatures

The peak that belonged to Orthorhombic ZrO_2 was detected at 415 cm^{-1} [30]. The peaks that belonged to cubic ZrO_2 were detected at 454 cm^{-1} [29]. The peak that belonged to GeO_2 were detected at 167 cm^{-1} for 700 and 800 °C samples. The numbers of GeO_2 peak increased as the oxidation/nitridation temperature increased. Extra GeO_2 peaks found in 800 °C samples were 263, 444, and 515 cm^{-1} [31, 32]. Ge_3N_4 peaks were detected at 202 and 455 cm^{-1} for 800 °C samples [33, 34]. These results were in conformity with the *J–V* characteristics where GeO_2 was detected for the samples oxidized/nitridation above 700 °C and Ge_3N_4 was detected in 800 °C samples.

3.4 XRD analysis

Figure 4 shows XRD patterns of samples oxidized/nitridation at various temperatures, from 49° to 56°. Several structures of ZrO_2 were detected. The orthorhombic ZrO_2 was found at around 51.21°, 52.71°, and 52.87°, corresponding to (151), (020), and (142) planes, respectively. These peaks are matched by ICSD with reference code 98-017-3960 and 98-005-6696. The tetragonal ZrO_2 was found at around 51.91° and 52.04° corresponding to (112) and (020) planes, respectively. These peaks are matched by ICSD with reference code 98-009-2092. The cubic ZrO_2 was found at around 51.32° corresponding to (022) planes. This peak is matched by ICSD with reference code 98-018-5123. The monoclinic ZrO_2 was found at around 51.03° corresponding to (12$\bar{2}$) planes. This peak is matched by ICSD with reference code 98-065-9226. On the other hand, the hexagonal $O_{0.27}Zr$ was found at around 51.41° corresponding to (026) planes. This peak is matched by ICSD with reference code 98-004-2986. The tetragonal GeO_8Zr_3 was found at around 51.61° corresponding to (220) planes. This peak is matched by ICSD with reference code 98-002-9263. The tetragonal Ge_4Zr_5 was found at around 51.78°, corresponding

to (117) planes. This peak is matched by ICSD with reference code 98-063-8154.

Figure 5 shows XRD patterns of samples oxidized/nitridation at various temperatures, from 10° to 80°. The peaks of hexagonal GeO_2, h-GeO_2 that were found in the 700 and 800 °C samples were around 20.55°, 25.94°, 35.99°, 38.02°, 39.47°, 41.80°, 44.90°, 48.27°, 48.66°, 53.35°, 56.31°, 58.84°, 61.65°, 66.04°, 67.03°, 73.81°, 76.32°, 77.27°, and 78.50° corresponding to (010), (011), (110), (102), (111), (020), (021), (003), (112), (202), (210), (211), (113), (122), (031), (302), (220), (213), and (221) planes, respectively. These peaks are matched by ICSD with reference code 98-001-6577. The peaks of orthorhombic Ge_3N_4, o-Ge_3N_4 that were found in the 700 and 800 °C samples were around 20.30°, 23.84°, 25.34°, 35.27°, 41.27°, 41.39°, 58.79°, 65.54°, 65.99°, 66.93°, 70.70°, and 73.89° corresponding to (101), (011), (111), (311), (202), (112), (430), (701), (313), (123), (413), and (721) planes, respectively. These peaks are matched by ICSD with reference code 98-015-6339. The GeO_2 and Ge_3N_4 were observed for sample 700 and 800 °C. It could be contributed to the diffusion of N_2O through ZrO_2 layer, which reacted with Ge and formed crystallization of GeO_2 and Ge_3N_4. These results were in conformity with the *J-V* characteristics, Raman spectroscopy analysis and OM analysis.

Williamson–Hall (W–H) plot analysis is used for evaluating the crystallite size (*D*) and microstrain (ε) [35–37]. The W–H as Eq. (1):

$$(\beta_S + \beta_D) \cos\theta = \frac{K\lambda}{D} + 4\varepsilon \sin\theta \tag{1}$$

where λ is the wavelength of the radiation; *K* is a constant, which is equal to 0.9; θ is the peak position; β_D is the peak width at half-maximum intensity; and β_S is the peak width at half-maximum intensity. Based on Eq. (1), one plots a graph of $(\beta_D + \beta_S) \cos\theta$ versus $4 \sin\theta$. Microstrain is the gradient,
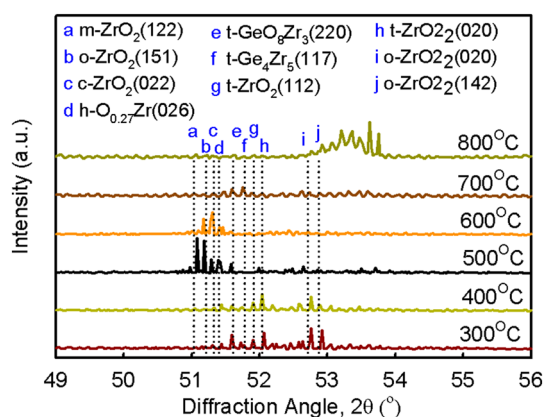

Fig. 4 XRD patterns of samples oxidized/nitridation at various temperatures form 49° to 56°
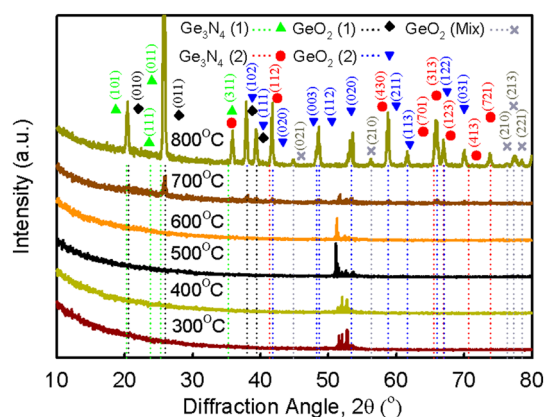

Fig. 5 XRD patterns of oxidized/nitridation at various temperatures form 10° to 80°

whereas $K\lambda/D$ is the intercept of the graph, from which D can be calculated as Eq. (2):

$$D = \frac{K\lambda}{y \ intercept} \tag{2}$$

Crystallite sizes of ZrO_2, $O_{0.27}Zr$, Ge_4Zr_5, and GeO_8Zr_3 were not calculated by using W–H plot because the number of peaks was insufficient for study purposes. Figure 6 shows the W–H plot of h-GeO_2 and O-Ge_3N_4 for 700 °C and 800 °C samples. According to Fig. 6, the points were well distributed in the four groups.

The crystallite size of h-GeO_2 (type 1) of 700 and 800 °C samples were 26.15 and 26.21 nm, respectively. The microstrain of h-GeO_2 (type 1) of the 700 and 800 °C samples were -0.0036 and -0.0034, respectively. The crystallite size of h-GeO_2 (type 2) of the 700 and 800 °C samples were 19.30 and 20.02 nm, respectively. The microstrain of h-GeO_2 (type 2) of the 700 and 800 °C samples were -0.0089 and -0.0076, respectively. These results were similar with the O_2 ambient.

The crystallite size of O-Ge_3N_4 for sample of 700 °C was not calculated by using W–H plot because the number of peaks was insufficient for study purposes. The crystallite size of O-Ge_3N_4 (type 1) of the 800 °C samples were 17.55 nm.

The microstrain of O-Ge_3N_4 (type 1) of the 800 °C samples were -0.0048. The crystallite size of O-Ge_3N_4 (type 2) of the 800 °C samples were 13.29 nm. The microstrain of O-Ge_3N_4 (type 2) of the 800 °C samples was -0.012.

Two type of GeO_2 and Ge_3N_4 crystallite size and microstrain were found indicates that two generating sources for GeO_2 and Ge_3N_4. This inference will be verified and discussed in a later section.

3.5 Thermal oxidation/nitridation mechanism

Figure 7a shows the schematic diagram of sputtered Zr film on Ge wafer before thermal oxidation. For the 300, 400, 500, and 600 °C samples, the N_2O directly reacted with the Zr film which was deposit by sputtering according to Eqs. (3) and (4) [38] and formed the ZrO_2 dielectric as shown in Fig. 7b.

$$Zr^+ + N_2O \rightarrow ZrO^+ + N_2 \tag{3}$$

$$ZrO^+ + N_2O \rightarrow ZrO_2^+ + N_2 \tag{4}$$

For the 700 and 800 °C samples, the samples thermally oxidized/nitridation according to the 3-step reactions, as shown in Fig. 7c. In high-temperature ambient, the N_2O received enough energy to diffuse through ZrO_2 dielectric layer and reacted with the Ge wafer. GeO_2 film formed on the surface of Ge wafer was assumed as equation Eqs. (5) and (6). After the GeO_2 formed, GeO_2 will react with Ge wafer, and GeO gas was generated according to Eq. (7) [9, 39]. The GeO gas diffused outward and reacted with N_2O in atmosphere. After that, another GeO_2 film was formed on the ZrO_2 assumed to be according to Eq. (8).

$$Ge^+ + N_2O \rightarrow GeO^+ + N_2 \tag{5}$$

$$Ge^+ + N_2O \rightarrow GeO_2^+ + N_2 \tag{6}$$

$$3GeO_2 + 3Ge \rightarrow 6GeO(g) \tag{7}$$

$$GeO(g) + N_2O \rightarrow GeO_2 + N_2 \tag{8}$$
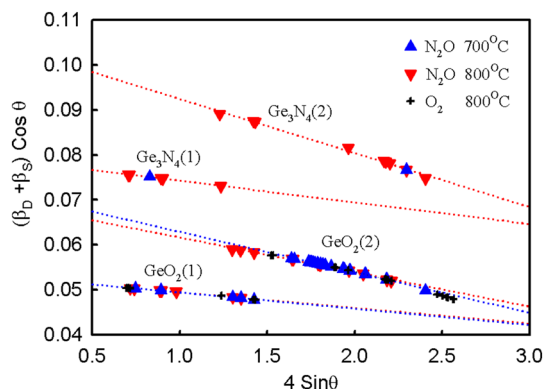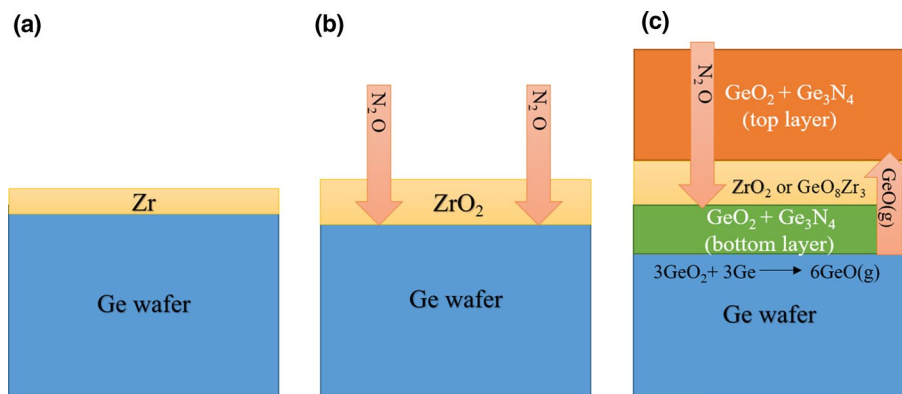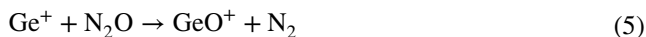
Fig. 6 W–H plot of GeO_2 and Ge_3N_4 for samples 700 and 800 °C

Fig. 7 Schematic diagram of thermal oxidation/nitridation mechanism. **a** Sputtering Zr on Ge wafer, **b** Zr oxidation to be ZrO_2 (for sample 300, 400, 500 and 600 °C), and **c** N_2O pass ZrO_2, GeO_2 and Ge_3N_4 generated (for sample 700 and 800 °C)

(a)

Zr

Ge wafer

(b)

N_2O | N_2O

ZrO_2

Ge wafer

(c)

N_2O

$GeO_2 + Ge_3N_4$ (top layer)

ZrO_2 or GeO_8Zr_3

$GeO_2 + Ge_3N_4$ (bottom layer)

GeO(g)

$3GeO_2 + 3Ge \longrightarrow 6GeO(g)$

Ge wafer

Because the Ge_3N_4 was found at Raman and XRD measurements, the reactive equation were assumes to be Eqs. (9) and (10).

$$4Ge + 2N_2O \rightarrow GeO_2 + Ge_3N_4 \qquad (9)$$

$$8GeO + 2N_2O \rightarrow 5GeO_2 + Ge_3N_4 \qquad (10)$$
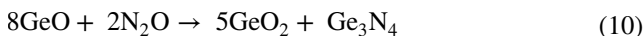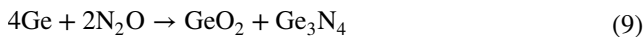
From the analysis of the two layers of GeO_2 and the two layers of Ge_3N_4, which are similar with the O_2 ambient, the absolute value of microstrain for the top layer will be less than the bottom layer. Therefore, h-GeO_2 (type 1) and O-Ge_3N_4 (type 1) at Fig. 6 were assumed to be the top layers, and the h-GeO_2 (type 2) and O-Ge_3N_4 (type 2) as the bottom layers.

3.6 HRTEM analysis

HRTEM analysis was performed to study the cross-section of the samples. Figure 8 shows the cross-section of the HRTEM images of the 400 and 500 °C samples. The thicknesses of ZrO_2 dielectric for the 400 and 500 °C samples were 5.6 and 6.8 nm, respectively. Assuming the thicknesses are in linear relationship with oxidation temperatures [40], by using 400 and 500 °C thicknesses, a regression line was shown at Fig. 9. Therefore, the thicknesses of the oxidized Zr thin films were approximately ranging from 4.4 to 8 nm from the 300 to 600 °C samples. The thicknesses for 700 and 800 °C will not be analyzed here because the film conditions were not appropriate for analysis. The ZrO_2 dielectric layer exhibits mainly an amorphous state with partial crystallized structure, and no IL was found between Ge wafer and ZrO_2 dielectric layer. The phenomenon of IL free will be discussed at Sect. 3.8.

3.7 XPS analysis

XPS analysis was performed for the evaluations of the structural and chemical properties of the ZrO_2 dielectric. Core-level spectra of Zr $3d$, Zr $3p$, Zr $3s$, Ge $3d$, Ge $3p$, Ge $3s$,
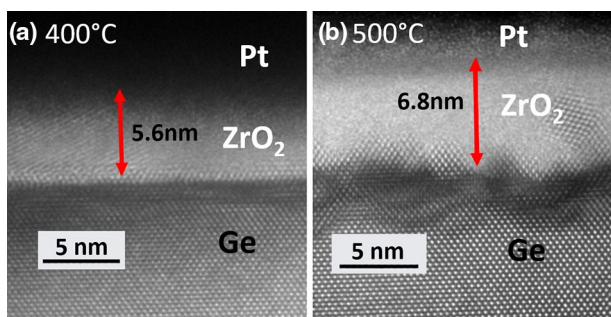

Fig. 8 Cross-sectional HRTEM images of samples oxidized/nitridation at temperatures 400 and 500 °C
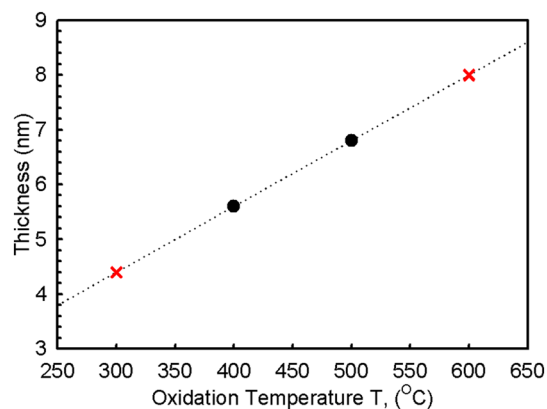

Fig. 9 Thickness of ZrO_2 dielectric of samples oxidized/nitridation at various temperatures

C $1s$, N $1s$, and O $1s$ were detected in the XPS wide scans. Narrow scans on Zr $3d$, Ge $3p$, and O $1s$ were also performed as a function of etching time for different oxidation/nitridation temperatures (300–600 °C) as shown in Figs. 10, 11, 12 and 13. Each spectrum was calibrated in respect to the carbon $1s$ (284.8 eV) state [41].

Figure 10 shows the narrow scan of Zr $3d$ for samples oxidized/nitridation at various temperatures from 300 to 600 °C. The positions of the peaks that belonged to Zr $3d_{5/2}$ were around 182.37–183.25 eV. The positions of peaks that belonged to Zr $3d_{3/2}$ were around 184.68–185.55 eV [42–45]. The peak positions of Zr $3d$ at the ZrO_2 surface were obviously lower than the inside for all samples. The detail mechanism will be discussed later. The peaks that belonged to Ge 3 s were observed for all samples. The peaks' height increased as etch time increases. As observed, after being etched around 840 s, the peaks that belonged to Zr 3d disappeared and left only Ge $3s$ peaks.

Figure 11 shows the narrow scan of Ge $3p$. The peaks that belonged to GeO_X of Ge $3p_{1/2}$ and Ge $3p_{3/2}$ were around 128.81–127.29 eV and 124.64–123.08 eV, respectively [46, 47], before etch. After being etched for 420–480 s, the peaks of Ge $3p_{1/2}$ and Ge $3p_{3/2}$ which belong to Ge were around 126 and 122 eV, respectively [44, 47]. After being etched for 420–480 s, a weak peak found at 118–119.7 eV, indicating that Ge-N bonds exist for all samples.

Figure 12 shows the narrow scan of O $1s$. The peaks that belonged to GeO_2 and ZrO_2 were found before etch for all samples at around 531.88–532.29 eV [48] and 530.67–531.12 eV [44, 49], respectively. After a certain level of etching, the peak of GeO_2 disappeared and left only the peak that belongs to ZrO_2. The details of the mechanism will be discussed in Sect. 3.8.

Figure 13 shows the narrow scan of N $1s$, no peak was found at the surface for all samples. After etch, a weak peak was found at around 404 eV which was assumed to be Ge–N.
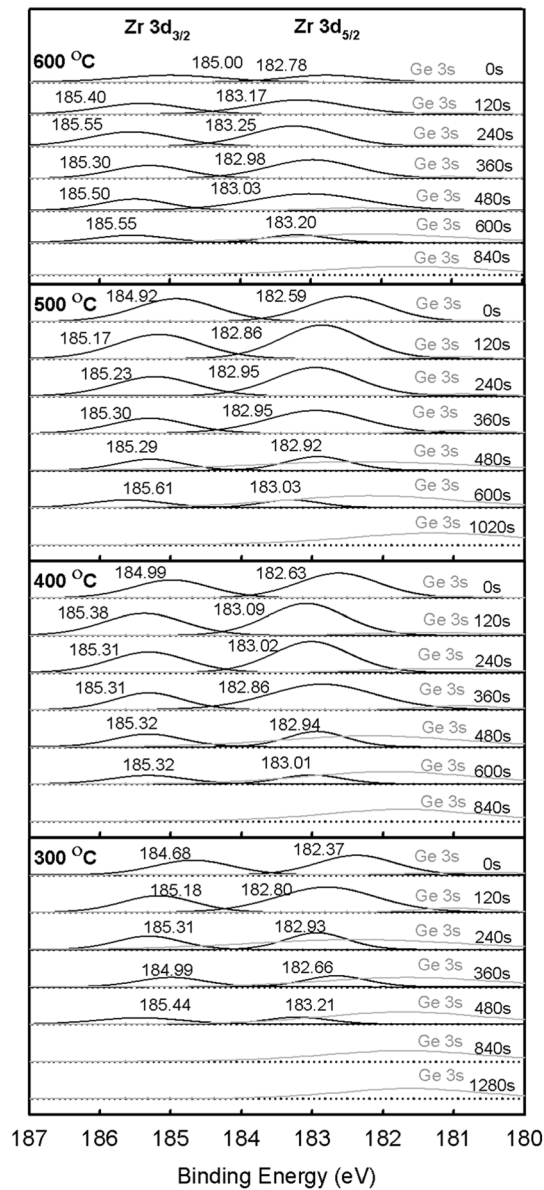
Fig. 10 Evolution of Zr 3d core level XPS spectra as a function of etching time for different oxidation/nitridation temperatures

Fig. 11 Evolution of Ge 3p core level XPS spectra as a function of etching time for different oxidation/nitridation temperatures

The same peaks were also detected at a deeper level of Ge wafer.

Figure 14 shows Zr $3d_{3/2}$ narrow scan peak position of samples oxidized/nitridation at various temperatures at various etching times. The fully oxidized line was plotted at 185.3 eV [45, 50]. The surface of ZrO_2 dielectric was under oxidation for all samples, it may be that Ge atom accumulation at the surface and combined with oxygen atom of existing ZrO_2 and induced the ZrO_2 under oxidation. For the 300 °C sample, mainly ZrO_2 under oxidation and the oxidation level increase when the temperature increases except the for 500 °C samples. This phenomenon was similar with the O_2 ambient. For the 600 °C sample, the result shows mainly
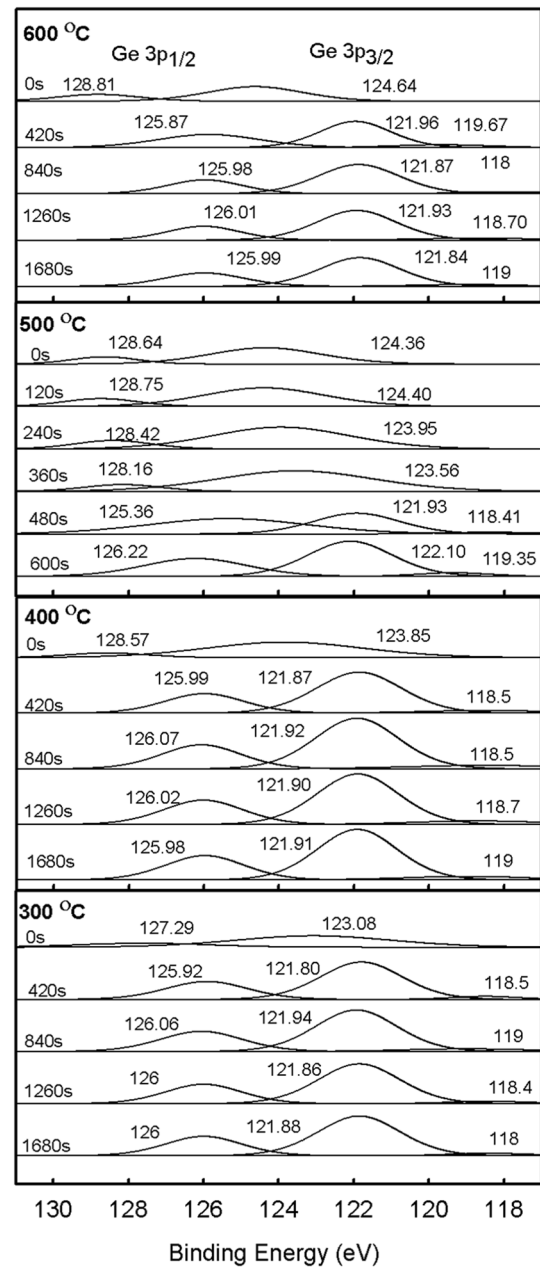
ZrO_2 overoxidation. The sample of 400 °C was the sample nearest to the full oxidation line, thus having the highest electrical breakdown fields compared with the other samples. For 300 and 500 °C samples, the ZrO_2 overoxidization is near Ge interface region. It could be that the Ge atoms diffused up during the cooling process, leaving excess O atoms causing ZrO_2 overoxidation. The details of the mechanism will be discussed at Sect. 3.8.

Figure 15 shows O 1s narrow scan of samples oxidized/nitridation at 400 °C. The back color line shows the original
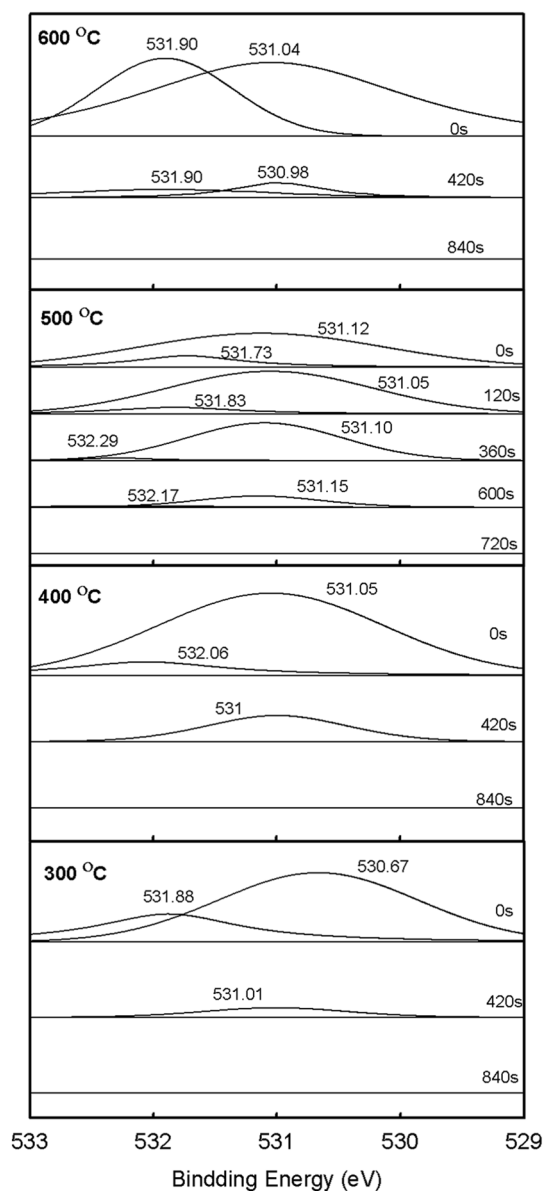
Fig. 12 Evolution of O 1*s* core level XPS spectra as a function of etching time for different oxidation/nitridation temperatures

Fig. 13 Evolution of N 1*s* core level XPS spectra as a function of etching time for different oxidation/nitridation temperatures

measurement line including noise. The peak position of GeO_2 was located at around 532.06 eV which was labeled as a green color line. The peak position of ZrO_2 was located at around 531.05 eV which was labeled as a red color line. The blue color shows the peak merge with ZrO_2 and GeO_2. Hence, when GeO_2 increase, the peak will shift to the left and shift to right when the ZrO_2 increases. Figure 16a was drawn based on this concept used to monitor the Ge atom arrangement in the ZrO_2. The GeO_2 and ZrO_2 binding energy were assumed to be 532.2 eV [51, 52] and 530.8 eV [53], respectively. As shown in Fig. 16a, the sample of 600 °C has the highest Ge atom in the ZrO_2 and sequentially, were 500, 400 and 300 °C. Obviously, the number of Ge atom diffused
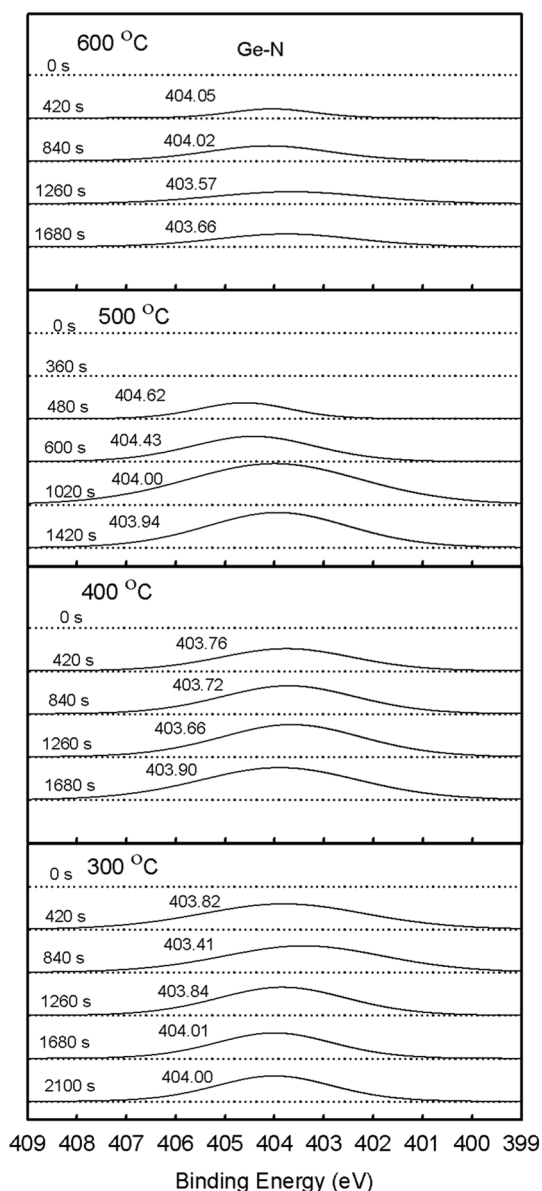
to ZrO_2 increase as the oxidation temperature increases. For the 500 and 600 °C samples, the concentration of Ge atoms increases at the interface of ZrO_2 and Ge wafer. Figure 16b shows the 400 °C sample cross-sectional HRTEM images, which correspond with Fig. 16a. A possible of mechanism will be discussed at the next section.

3.8 Ge diffused and rearrange mechanism

When Ge atoms diffuse to ZrO_2 region, it should be travelling in random thermal motion [54]. However, the XPS result has shown that the Ge atoms were accumulating at both sides of ZrO_2, indicating that another factor does
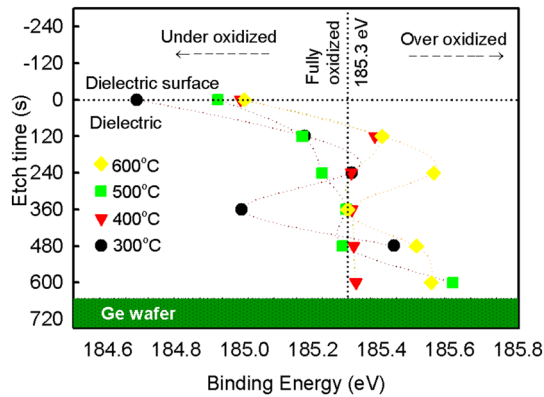
Fig. 14 XPS Zr $3d_{3/2}$ narrow scan peak position of samples oxidized/nitridation at various temperatures and various etching time
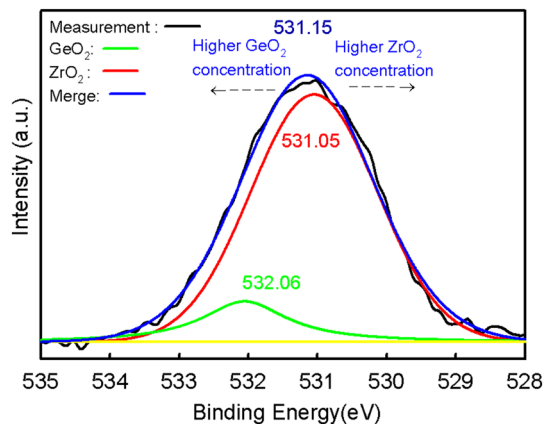

Fig. 15 XPS O $1s$ narrow scan of 400 °C sample

exist to influence the way the Ge atom behaves. The factor could be the thermal gradient during cooling appear to make Ge rearrange. As ZrO_2 has low thermal conductivity of less than 4 W m^{-1} K^{-1} above 500 °C [55], high thermal gradient formed during the cooling process. Figure 17a shows the schematic diagram during thermal process, the Ge atoms diffuse to ZrO_2 film with Ge concentration being highest near Ge surface and lowest Ge concentration at ZrO_2 surface [56]. Figure 17b shows the schematic diagram of Ge distribution during cooling process. The Ge atom at the center region was at random thermal motion due to higher temperature at the center of ZrO_2. The atoms diffused near the edge of the ZrO_2 which stayed stagnant due to the high thermal gradient. Hence, the Ge atoms accumulate at both sides of ZrO_2 eventually. As explained above, the thermal motion of Ge atoms during cooling will result in an IL-free phenomenon.

4 Conclusions

The activation energies of N_2O are higher than O_2, thus explaining the stable film performance at N_2O ambient than O_2 ambient at temperature above 600 °C. The ZrO_2 dielectric film was unstable for temperatures above 700 °C on Ge wafer in N_2O ambient. Ge diffusion was observed during oxidation process. A possible mechanism of Ge atomic diffusion and its rearrangement in ZrO_2 has been proposed and explicated. The sample of 400 °C was closest to the full oxidation, and electrical characterization has shown that the 400 °C sample has the highest electrical breakdown fields.
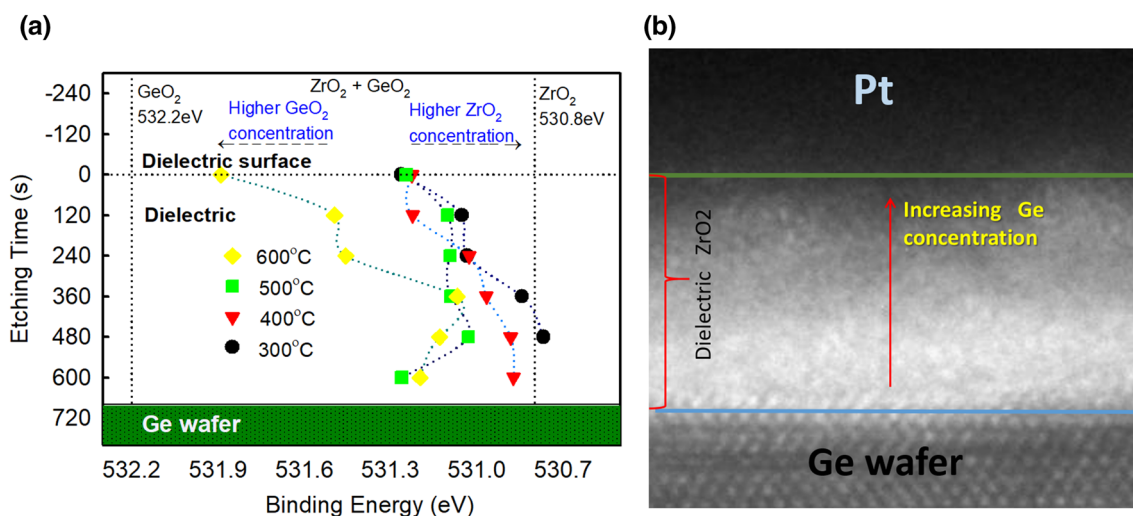

Fig. 16 a XPS O $1s$ narrow scan peak position of samples oxidized/nitridation at various temperatures and various etching time and **b** 400 °C sample cross-sectional HRTEM images
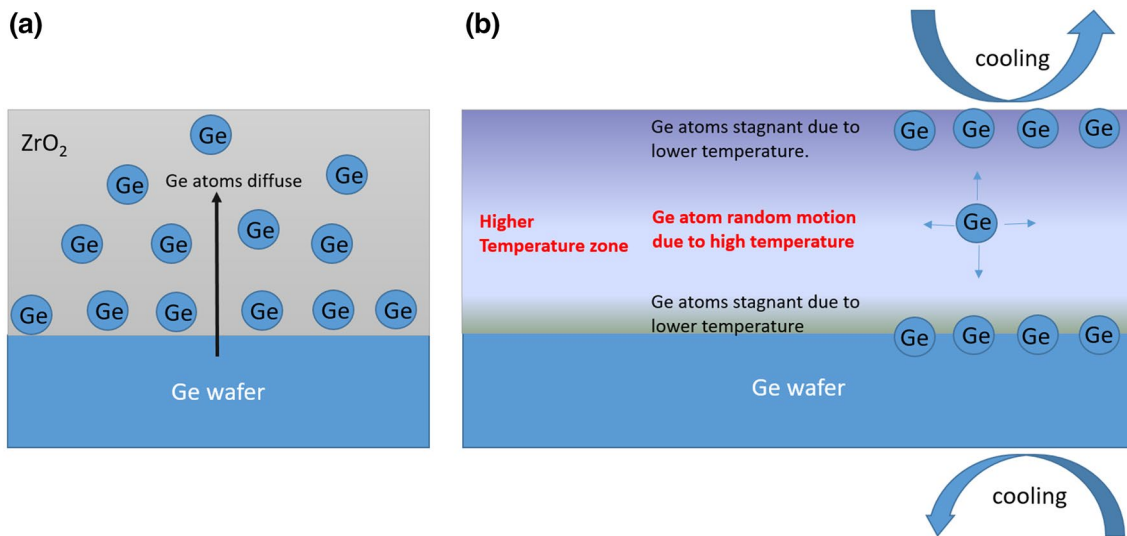
Fig. 17 Schematic diagram of Ge diffuse **a** during thermal process and **b** during cooling process

References

1. X.R. Wang et al., Annealing effect on the metal gate effective work function modulation for the Al/TiN/SiO₂/p-Si structure. Microelectron. Eng. **88**(5), 573–577 (2011)
2. V.E. Vamvakas et al., Correlation between infrared transmission spectra and the interface trap density of SiO₂ films. Microelectron. Reliab. **47**(4–5), 834–837 (2007)
3. D.G. Park, T.K. Kim, Effects of fluorine and chlorine on the gate oxide integrity of W/TiN/SiO₂/Si metal-oxide-semiconductor structure. Thin Solid Films **483**(1–2), 232–238 (2005)
4. T. Sakurai et al., Electrical properties of the silicon oxide/Si structure formed with perchloric acid at 203 °C. Solid State Commun. **118**(8), 391–394 (2001)
5. C.A. Mack, Fifty years of Moore's law. IEEE Trans. Semicond. Manuf. **24**(2), 202–207 (2011)
6. S.E. Thompson, S. Parthasarathy, Moore's law: the future of Si microelectronics. Mater. Today **9**(6), 20–25 (2006)
7. V.K. Arora, D.C.Y. Chek, M.L.P. Tan, *The Role of Ballistic Mobility and Saturation Velocity in Performance Evaluation of a Nano-CMOS Circuit*. 2009 International Conference on Emerging Trends in Electronic and Photonic Devices and Systems (Electro-2009) (2009), p. 14
8. R. Pillarisetty, Academic and industry research progress in germanium nanodevices. Nature **479**(7373), 324–328 (2011)
9. Y. Kamata, High-k/Ge MOSFETs for future nanoelectronics. Mater. Today **11**(1–2), 30–38 (2008)
10. Y.H. Lee et al., *Prediction of Logic Product Failure Due to Thin-Gate Oxide Breakdown*. 2006 IEEE International Reliability Physics Symposium Proceedings—44th Annual (2006), p. 18
11. P.W. Peacock, J. Robertson, Bonding, energies, and band offsets of Si–ZrO₂ and HfO₂ gate oxide interfaces. Phys. Rev. Lett. **92**(5), (2004)
12. K.H. Goh, A.S.M.A. Haseeb, Y.H. Wong, Physical and electrical properties of thermal oxidized Sm₂O₃ gate oxide thin film on Si substrate: influence of oxidation durations. Thin Solid Films **606**, 80–86 (2016)
13. K. Hetherin, S. Ramesh, Y.H. Wong, Formation of neodymium oxide by thermal oxidation of sputtered Nd thin film on Si substrate. J. Mater. Sci: Mater. Electron. **28**(16), 11994–12003 (2017)
14. C.K. Maiti et al., Electrical characterization of TiO₂ gate oxides on strained-Si. Microelectron. Eng. **72**(1–4), 253–256 (2004)
15. M. Tapajna et al., Gate oxide thickness dependence of the leakage current mechanism in Ru/Ta₂O₅/SiON/Si structures. Semicond. Sci. Technol. **25**(7), 075007 (2010)
16. C. Lee et al., The electrical and physical analysis of Pt gate/Al₂O₃/p-Si (100) with dual high-k gate oxide thickness for deep submicron complementary metal-oxide-semiconductor device with low-power and high reliability. J. Electron. Mater. **34**(8), 1104–1109 (2005)
17. B.W. Busch et al., Interface reactions of high-kappa Y₂O₃ gate oxides with Si. Appl. Phys. Lett. **79**(15), 2447–2449 (2001)
18. Y.H. Wong, K.Y. Cheong, ZrO₂ thin films on Si substrate. J. Mater. Sci: Mater. Electron. **21**(10), 980–993 (2010)
19. C.C. Li et al., Improved electrical characteristics of Ge pMOSFETs with ZrO₂/HfO₂ stack gate dielectric. IEEE Electron. Device Lett. **37**(1), 12–15 (2016)
20. Z.C. Lei et al., Effect of oxidation temperature on physical and electrical properties of ZrO₂ thin-film gate oxide on Ge substrate. Thin Solid Films **642**, 352–358 (2017)
21. R. De Almeida, I.J.R. Baumvol, Reaction–diffusion in high-k dielectrics on Si. Surf. Sci. Rep. **49**(1–3), 1–114 (2003)
22. S. Dimitrijev et al., in *Recent Major Advances in SiC*, ed. by W.J. Choyke, H. Matsunami, G. Pensl (Taylor & Francis, New York, 2003)
23. M.L. Campbell, R.E. Mcclean, Kinetics of Neutral transition-metal atoms in the gas-phase—oxidation reactions of Ti(a(3)F) from 300-K to 600-K. J. Phys. Chem. **97**(30), 7942–7946 (1993)
24. K. Maeda et al., Dependence of activity and stability of germanium nitride powder for photocatalytic overall water splitting on structural properties. Chem. Mater. **19**(16), 4092–4097 (2007)

25. Y.G. Lee et al., Effect of high-pressure ammonia treatment on the activity of Ge_3N_4 photocatalyst for overall water splitting. J. Phys. Chem. B **110**(35), 17563–17569 (2006)

26. Y. Leng, *Materials Characterization: Introduction to Microscopic and Spectroscopic Methods* (Wiley, New York, 2009)

27. Q. Tong et al., Rhenium-promoted $Pt/WO_3/ZrO_2$: an efficient catalyst for aqueous glycerol hydrogenolysis under reduced H-2 pressure. RSC Adv. **6**(89), 86663–86672 (2016)

28. M. Rawat et al., Micro-Raman and electronic structure study on kinetics of electronic excitations induced monoclinic-to-tetragonal phase transition in zirconium oxide films. RSC Adv. **6**(106), 104425–104432 (2016)

29. S. Vasanthavel, S. Kannan, Structural investigations on the tetragonal to cubic phase transformations in zirconia induced by progressive yttrium additions. J. Phys. Chem. Solids **112**, 100–105 (2018)

30. G. Sponchia et al., Orthorhombic phase stabilization and transformation phase process in zirconia tantalum-doped powders and spark plasma sintering systems. J. Eur. Ceram. Soc. **37**(10), 3393–3401 (2017)

31. A. Lignie et al., Raman study of alpha-quartz-type $Ge_{1-x}Si_xO_2$ $(0 < x < = 0.067)$ single crystals for piezoelectric applications. RSC Adv. **5**(69), 55795–55800 (2015)

32. G. Kartopu et al., On the origin of the 2.2–2.3 eV photoluminescence from chemically etched germanium. J. Lumin. **101**(4), 275–283 (2003)

33. P. Kroll, Pathways to metastable nitride structures. J. Solid State Chem. **176**(2), 530–537 (2003)

34. S.K. Deb et al., The Raman spectra of the hexagonal and cubic (spinel) forms of Ge_3N_4: an experimental and theoretical study. Solid State Commun. **114**(3), 137–142 (2000)

35. X. Fan, H. Liu, X. Zhang, Identification of optimal ALD process conditions of Nd_2O_3 on Si by spectroscopic ellipsometry. Appl. Phys. A **114**(2), 545–550 (2014)

36. A. Laha et al., Epitaxial multi-component rare earth oxide for high-K application. Thin Solid Films **515**(16), 6512–6517 (2007)

37. T.-M. Pan, J.-D. Lee, W.-W. Yeh, Influence of oxygen content on the structural and electrical characteristics of thin neodymium oxide gate dielectrics. J. Appl. Phys. **101**(2), 024110 (2007)

38. J. Moureau et al., High accuracy measurements of Mo isotopes by MC-ICPMS with in situ Mo/Zr separation using N_2O in a collision reaction cell. J. Anal. At. Spectrom. **23**(11), 1538–1544 (2008)

39. L. Khomenkova, Effect of Ge content on the formation of Ge nanoclusters in magnetron-sputtered GeZrOx-based structures. Nanoscale Res. Lett. **12**. (2017)

40. S.K. Sahari et al., *Kinetics of Thermally Oxidation of Ge(100) Surface*. 15th International Conference on Thin Films (Ictf-15). (2013), p. 417

41. https://xpssimplified.com/elements/carbon.php

42. Y.H. Wong, K.Y. Cheong, Thermal oxidation and nitridation of sputtered Zr thin film on Si via N_2O gas. J. Alloys Compd. **509**(35), 8728–8737 (2011)

43. E. Marin et al., Wear and surface degradation of commercial ZTA femoral heads under boundary lubrication conditions. J. Mech. Behav. Biomed. Mater. **65**, 616–626 (2017)

44. F.M. John et al., *Handbook of X-ray Photoelectron Spectroscopy* (Perkin-Elmer Corporation Physical Electronics Division, Eden Prairie, 1992)

45. S. Sinha, S. Badrinarayanan, A. Sinha, Interaction of oxygen with $Zr_{76}Fe_{24}$ metglass: an X-ray photoelectron spectroscopy study. J. Less Common Met. **125**, 85–95 (1986)

46. O. Bethge et al., Stability of La_2O_3 and GeO_2 passivated Ge surfaces during ALD of ZrO_2 high-k dielectric. Appl. Surf. Sci. **258**(8), 3444–3449 (2012)

47. Q. Xie et al., Germanium surface passivation and atomic layer deposition of high-k dielectrics-a tutorial review on Ge-based MOS capacitors. Semicond. Sci. Technol. **27**(7), (2012)

48. F. Wei, H.L. Tu, J. Du, Twin-free (111)-oriented epitaxial $Nd_2Hf_2O_7$ thin films on Ge(111) for high-k dielectrics. J. Phys. D **42**(18), 185301 (2009)

49. L.G. Kim et al., Enhanced electrooptical characteristics of twisted nematic liquid crystal display with ZrO_2 thin films. IEEE Electron. Device Lett. **33**(8), 1153–1155 (2012)

50. Q.C. Zhang et al., Preparation and characterization of polymer-derived Zr/Si/C multiphase ceramics and microspheres with electromagnetic wave absorbing capabilities. J. Eur. Ceram. Soc. **37**(5), 1909–1916 (2017)

51. M.K. Bera et al., TiO_2/GeO_xN_y stacked gate dielectrics for Ge-MOSFETs. Semicond. Sci. Technol. **22**(12), 1352–1361 (2007)

52. R.T. Kouzes, Z. Zhu, M.H. Engelhard, Germanium-76 Sample Analysis: Revision 3. 2011, Pacific Northwest National Laboratory (PNNL), Richland, WA (US), Environmental Molecular Sciences Laboratory (EMSL)

53. X. Guo, Y.-Q. Sun, K. Cui, Darkening of zirconia: a problem arising from oxygen sensors in practice. Sens. Actuators B **31**(3), 139–145 (1996)

54. S.M. Sze, *Semiconductor Devices: Physics and Technology* (Wiley, New York, 2008)

55. Q. Mistarihi et al., Fabrication of ZrO2-based nanocomposites for transuranic element-burning inert matrix fuel. Nuclear Eng. Technol. **47**(5), 617–623 (2015)

56. F. Boucard et al., *A Model for Boron TED in Silicon: Full Couplings of Dopant with Free and Clustered Interstitials*. MRS Online Proceedings Library Archive. (2002), p. 717